Journal of Peridynamics and Nonlocal Modeling (2019) 1:56–73
https://doi.org/10.1007/s42102-018-0001-0

ORIGINAL ARTICLES

Discrete Micromodulus Functions for Reducing Wave Dispersion in Linearized Peridynamics

Raymond A. Wildman[1]

Received: 15 March 2018 / Accepted: 24 July 2018 / Published online: 29 October 2018

Abstract
Typical implementations of peridynamics use a constant or tapered micromodulus (or influence) function, the choice of which has been shown to have a large impact on the dispersion relation. In this work, a method for computing micromodulus function values at discretized points within a node's horizon is presented for linearized peridynamics. The technique involves constructing a system of equations representing the desired dispersion relation and solving for the micromodulus function coefficients at discretized node locations. Both 1D and 2D formulations are presented. A straightforward implementation of the method results in negative coefficients, which improve wave propagation accuracy, but results in unstable solutions of fracture problems using a bond-breakage scheme. Two methods for addressing this issue are discussed: A hybrid method that uses a constant micromodulus function after damage has occurred at a node, and a constrained solution that results in only positive coefficients. The dispersion properties of the method are examined in detail, including the numerical anisotropy in 2D. Finally, results for wave propagation in 1D and 2D, static fracture, and dynamic fracture are given.

Keywords Dispersion · Fracture · Elastic wave propagation

1 Introduction

Peridynamics is a nonlocal reformulation of continuum mechanics which allows for the treatment of discontinuities in the displacement [26, 27], and has seen effective use in the simulation of dynamic fracture problems [8, 12]. Peridynamics has two main formulations: bond-based, which is restricted to certain classes of material models (and includes restrictions on Poisson's ratio for linear elastic materials); and state-based, which generalizes peridynamics to a wide range of material classes [7, 28]. In addition, peridynamics has been extended to other fields, such as thermomechanics [20], diffusion [3], porous flow [16, 21], and electromigration [9].

For problems involving wave propagation, however, peridynamics suffers from anomalous wave dispersion, which can adversely affect the accurate simulation of the time-dependent deformation of linear elastic materials [2, 4, 24]. The effects of wave dispersion are apparent in peridynamics simulations in the form of slow wave speeds, spurious oscillations, and wave damping [6, 10, 30, 31, 35]. The nonlocality inherent in peridynamic formulations, while allowing for the incorporation of discontinuities and singularities in the displacement field, is the main cause of the anomalous dispersion. Two main approaches exist for addressing dispersion, hybrid techniques, which use finite element or finite difference methods in the bulk of a material and peridynamics at fracture surfaces [1, 13, 25, 33, 34], and alternative influence functions (rather than the standard constant function) [4, 24]. The micromodulus or influence function appears in the peridynamic integral formulation and is typically constant or tapered and radially symmetric. The purpose of this work is to extend the concept of using the micromodulus function to alter the dispersion characteristics to a discrete form wherein coefficients of the micromodulus function are computed at discretized node locations to match a given dispersion relation. A similar approach may be found in Weckner and Silling [32], where nonlocal constitutive models were derived using dispersion relations for dispersive materials.

The discrete micromodulus function used here will be computed by using a planewave representation of

✉ Raymond A. Wildman
raymond.a.wildman.civ@mail.mil

[1] US Army Research Laboratory, 6300 Rodman Rd., Aberdeen Proving Ground, MD, USA

the displacement. Upon substitution into the discretized peridynamic equation of motion, a system of equations can be formed that enforces a specific dispersion relation at a given number of frequencies (or wavelengths). The method in 1D is straightforward and results in a set of coefficients that resemble higher order finite difference coefficients. In fact, similar techniques may be found in the finite difference literature [14, 15, 29]. In 2D, the method is similar though complicated by the vector displacement and two types of waves: longitudinal and shear.

An unfortunate side effect of the improved accuracy is that some of the micromodulus function coefficients are negative, which causes stability issues when used with a bond-breakage scheme for dynamic fracture. Two methods for addressing this issue are discussed, namely, a hybrid technique that uses the discrete micromodulus function in the bulk and a constant micromodulus function at fracture surfaces, and a constrained solution approach that places a lower limit on the micromodulus function values.

The remainder of this paper is organized as follows: First, Section 2 details the formulation of the method in 1D and 2D. Second, Section 3 discusses several implementation details including solution of the linear systems and stabilization methods for modeling damage. In Section 4, several examples of dispersion curves are given of the discretized method, including plots of the numerical anisotropy in 2D. Section 5 gives numerical examples including 1D and 2D wave propagation as well as static and dynamic fractures. Finally, conclusions are given in Section 6.

2 Formulation

Bond-based peridynamics defines the following equation of motion for a point $\mathbf{x}$ with density $\rho(\mathbf{x})$ and body-force $\mathbf{b}(\mathbf{x})$

$$\rho(\mathbf{x})\frac{\partial^2}{\partial t^2}\mathbf{u}(\mathbf{x}) = \int_{\mathcal{H}} \boldsymbol{f}(\mathbf{u}(\mathbf{x}') - \mathbf{u}(\mathbf{x}), \mathbf{x}' - \mathbf{x})\mathrm{d}V_{\mathbf{x}'} + \mathbf{b}(\mathbf{x}), \quad (1)$$

with $\mathcal{H}$ representing the neighborhood of $\mathbf{x}$, which is typically spherical with radius δ. Letting $\boldsymbol{\eta} = \mathbf{u}(\mathbf{x}') - \mathbf{u}(\mathbf{x})$ and $\boldsymbol{\xi} = \mathbf{x}' - \mathbf{x}$, and expressing the stretch s in terms of the deformed bond vector $\mathbf{y} = \boldsymbol{\xi} + \boldsymbol{\eta}$ as

$$s = \frac{|\mathbf{y}| - |\boldsymbol{\xi}|}{|\boldsymbol{\xi}|}, \quad (2)$$

the force-function is given as

$$\boldsymbol{f}(\mathbf{y}, \boldsymbol{\xi}) = c(\boldsymbol{\xi}) s \frac{\mathbf{y}}{|\mathbf{y}|}, \quad (3)$$

which models a linear elastic solid for small displacements [27]. A linearized version of Eq. 3 is given by

$$\boldsymbol{f}(\mathbf{y}, \boldsymbol{\xi}) = c(\boldsymbol{\xi}) \frac{\boldsymbol{\xi} \otimes \boldsymbol{\xi}}{|\boldsymbol{\xi}|^3} \boldsymbol{\eta}. \quad (4)$$

In Eqs. 3 and 4, the micromodulus function $c(\boldsymbol{\xi})$ represents a bond's elastic stiffness, which may be expressed in terms of the elastic constitutive properties (e.g., Young's modulus and Poisson's ratio) by comparing the strain energy resulting from an isotropic strain with that of a classically elastic solid.

For a circular horizon (in 2D plane strain), the micromodulus function with a constant influence function is given as [19]

$$c(\boldsymbol{\xi}) = \frac{6\lambda}{\pi\delta^3\nu} H(\delta - |\boldsymbol{\xi}|), \quad (5)$$

where ν is Poisson's ratio, λ is Lamé's first parameter, and $H(\cdot)$ is the Heaviside step function. Comparing the strain energies of the classical and peridynamic models for a purely deviatoric deformation reveals a Poisson ratio $\nu = \frac{1}{4}$ in 3D, and $\nu = \frac{1}{4}$ and $\nu = \frac{1}{3}$ for 2D plane strain and plane stress, respectively.

The main idea of the proposed approach is to compute a discrete micromodulus function that matches a particular dispersion curve at a given set of frequencies. A 1D formulation will be given first as its presentation is simpler. Subsequently, a 2D formulation is given, which is complicated by the need for matching two wave speeds—longitudinal and shear.

2.1 1D Formulation

The linearized, spatially discretized peridynamic equation of motion in 1D is given by

$$\rho\frac{\partial^2}{\partial t^2}u_m = E\sum_{n=-N}^{N} c_n \frac{u_{m+n} - u_m}{|x_{m+n} - x_m|} v_n, \quad (6)$$

where the c_n are the discretized values of the micromodulus function, and v_n is the length associated with a node that appears from discretizing the integral. Further assumed in Eq. 6 is a uniform grid spacing of Δx, so that $x_m = m\Delta x$, and that the equation is enforced at the integration nodes. The horizon size in this discretization is $\delta = N\Delta x$, so that each node's neighborhood (away from the boundary) contains $2N + 1$ bonds. Figure 1 gives an example of this discretization with $N = 3$.

Now, a planewave representation will be used for the displacement, given as

$$u = e^{i\omega t}e^{ikx}, \quad (7)$$

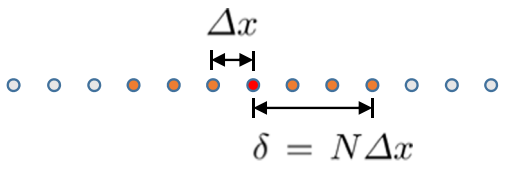

Fig. 1 Node locations in 1D with horizon

and is substituted into Eq. 6 giving

$$-\rho\omega^2 e^{i\omega t}e^{ikx_m} = E\sum_{n=-N}^{N}\frac{c_n v_n}{|n|\Delta x}(e^{i\omega t}e^{ik(m+n)\Delta x} - e^{i\omega t}e^{ikm\Delta x}). \tag{8}$$

Next, without loss of generality, we can consider only the equation at $m = 0$ and split the summation as

$$-\frac{\rho}{E}\omega^2 = \sum_{n=-N}^{-1}\frac{c_n v_n}{|n|\Delta x}(e^{-ik|n|\Delta x} - 1) + \sum_{n=1}^{N}\frac{c_n v_n}{|n|\Delta x}(e^{ik|n|\Delta x} - 1). \tag{9}$$

Assuming that the coefficients are symmetric (i.e., $c_{-n} = c_n$) allows the summations to be combined as

$$-\frac{\rho}{E}\omega^2 = \sum_{n=1}^{N}\frac{2c_n v_n}{|n|\Delta x}(\cos(k|n|\Delta x) - 1). \tag{10}$$

Rather than separating the node length and micromodulus function values, $c_n v_n$ may be combined into one unknown, say $c_n v_n = C_n$, giving

$$-\frac{\Delta x\rho}{2E}\omega^2 = \sum_{n=1}^{N} C_n\frac{\cos(k|n|\Delta x) - 1}{|n|}. \tag{11}$$

Next, the linear dispersion relation $\omega^2 = k^2E/\rho$ may be used to eliminate ω, ultimately giving

$$-\frac{\Delta x k^2}{2} = \sum_{n=1}^{N} C_n\frac{\cos(k|n|\Delta x) - 1}{|n|}. \tag{12}$$

(Note that in this case a linear dispersion relation was assumed, though in future work different dispersion relations may be used to model dispersive materials as discussed in Weckner and Silling [32].) Equation 12 represents one equation with N unknown coefficients C_n. There are several techniques to form a full linear system, though here we simply choose N wavenumbers at which to enforce the equation. The choice of these wavenumbers should span a range to capture both long and short wavelength effects; thus, a small, but non-zero value is chosen as the minimum value for k and a significant fraction (approximately 40%) of the spatial Nyquist sampling rate is chosen for the maximum value. In between, a set of equally spaced values is used to complete the full set of N values.

2.2 2D Formulation

For a 2D Cartesian grid with spacings Δx and Δy and a (in general) rectangular-shaped horizon with dimensions $2N\Delta x$-by-$2M\Delta y$, the linearized and discretized peridynamic equation in 2D may be expressed as

$$\rho\frac{\partial^2\mathbf{u}_{ij}}{\partial t^2} = \sum_{m=-M}^{M}\sum_{n=-N}^{N} c_{ij,mn}\frac{\boldsymbol{\xi}_{ij,mn}\otimes\boldsymbol{\xi}_{ij,mn}}{|\boldsymbol{\xi}_{ij,mn}|^3}\boldsymbol{\eta}_{ij,mn}v_{ij,mn}, \tag{13}$$

where $\boldsymbol{\xi}_{ij,mn} = \mathbf{x}_{mn} - \mathbf{x}_{ij}$ and $\boldsymbol{\eta}_{ij,mn} = \mathbf{u}_{mn} - \mathbf{u}_{ij}$. As in the 1D case, the horizon size is dictated by the grid spacings and N and M, and the number of nodes in a horizon is given by $(2N + 1)(2M + 1)$. If a square horizon is assumed with equal grid spacing, then $M = N$, $\Delta x = \Delta y$, and $\delta = N\Delta x$, though here δ represents half the side length and not a radius. (Note that even though a square horizon is assumed, the micromodulus function may be expressed in a way as to form a standard, circular horizon by setting coefficients to 0 outside of a given radius.) Figure 2 illustrates the above quantities for a square horizon.

As before, without loss of generality, we may specify $\mathbf{x}_{ij} = \mathbf{0}$, and consider the equation with $i = j = 0$. The above can now be expressed as

$$\rho\frac{\partial^2\mathbf{u}_{00}}{\partial t^2} = \sum_{m=-M}^{M}\sum_{n=-N}^{N}\frac{C_{mn}}{|\mathbf{x}_{mn}|^3}\boldsymbol{\Xi}^{+}_{mn}\boldsymbol{\eta}_{mn}, \tag{14}$$

where, as before, the node area and coefficient are combined into C_{mn} and now $\boldsymbol{\eta}_{mn} = \mathbf{u}_{mn} - \mathbf{u}_{00}$, $\mathbf{x}_{mn}$ is given by

$$\mathbf{x}_{mn} = m\Delta x\hat{\mathbf{x}} + n\Delta y\hat{\mathbf{y}}, \tag{15}$$

which results in

$$\mathbf{x}_{mn}\otimes\mathbf{x}_{mn} = \begin{bmatrix} m^2\Delta x^2 & mn\Delta x\Delta y \\ mn\Delta x\Delta y & n^2\Delta y^2 \end{bmatrix} \equiv \boldsymbol{\Xi}^{+}_{mn}. \tag{16}$$

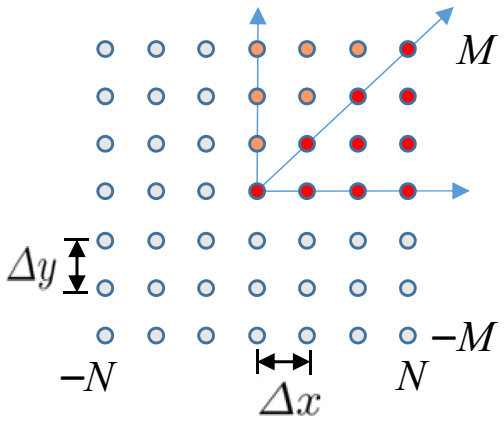

Fig. 2 Node locations in 2D for a square horizon. Red nodes indicate unique coefficients

Now, in 2D, the planewave representation of the displacement is given by the following

$$\mathbf{u} = A\hat{\mathbf{k}}e^{i\omega t}e^{i\mathbf{k}^{\mathrm{p}}\cdot\mathbf{x}} + B(\hat{\mathbf{z}}\times\hat{\mathbf{k}})e^{i\omega t}e^{i\mathbf{k}^{\mathrm{s}}\cdot\mathbf{x}}, \tag{17}$$

where $\mathbf{k}^{\mathrm{p}}$ and $\mathbf{k}^{\mathrm{s}}$ are the wave vectors for the longitudinal and shear waves respectively and $k_{\mathrm{x}}^{\mathrm{p}} = \mathbf{k}^{\mathrm{p}}\cdot\hat{\mathbf{x}}$, etc. Further, the wavenumbers are given by

$$|\mathbf{k}^{\mathrm{p}}|^2 = \frac{\omega^2\rho}{\lambda+2\mu}, \tag{18}$$

$$|\mathbf{k}^{\mathrm{s}}|^2 = \frac{\omega^2\rho}{\mu}, \tag{19}$$

where μ is Lamé's second parameter and the wave vector direction may be given by the unit vector with angle θ

$$\hat{\mathbf{k}} = \frac{\mathbf{k}^{\mathrm{s}}}{|\mathbf{k}^{\mathrm{s}}|} = \frac{\mathbf{k}^{\mathrm{p}}}{|\mathbf{k}^{\mathrm{p}}|} = [\cos\theta, \sin\theta]^{\mathrm{T}}. \tag{20}$$

Substituting Eq. 17 into Eq. 14 and simplifying gives

$$\begin{aligned} -\omega^2\rho[A\hat{\mathbf{k}} + B(\hat{\mathbf{z}}\times\hat{\mathbf{k}})] = {} & A\sum_{m=-M}^{M}\sum_{n=-N}^{N}\frac{C_{mn}}{|\mathbf{x}_{mn}|^3}\boldsymbol{\Xi}_{mn}^{+}\hat{\mathbf{k}}(e^{ik_{\mathrm{x}}^{\mathrm{p}}m\Delta x}e^{ik_{\mathrm{y}}^{\mathrm{p}}n\Delta y} - 1) \\ & + B\sum_{m=-M}^{M}\sum_{n=-N}^{N}\frac{C_{mn}}{|\mathbf{x}_{mn}|^3}\boldsymbol{\Xi}_{mn}^{+}(\hat{\mathbf{z}}\times\hat{\mathbf{k}})(e^{ik_{\mathrm{x}}^{\mathrm{s}}m\Delta x}e^{ik_{\mathrm{x}}^{\mathrm{s}}n\Delta y} - 1). \end{aligned} \tag{21}$$

As with the 1D case, the coefficients are assumed to be symmetric, in this case about the $x = 0$ and $y = 0$ lines, meaning that one quadrant defines the set of unique coefficients. As we are only treating isotropic materials here, the coefficients could further be assumed symmetric about the $y = x$ line, though this will not be incorporated into the formulation as it can be enforced by using the appropriate wave directions when solving the system of equations. These assumptions result in

$$\begin{aligned} -\omega^2\rho[A\hat{\mathbf{k}} + B(\hat{\mathbf{z}}\times\hat{\mathbf{k}})] = {} & A\sum_{m=0}^{M}\sum_{n=0}^{N}h_{mn}\frac{C_{mn}}{|\mathbf{x}_{mn}|^3}\boldsymbol{\Xi}_{mn}^{+}\hat{\mathbf{k}}[\cos(k_{\mathrm{x}}^{\mathrm{p}}m\Delta x + k_{\mathrm{y}}^{\mathrm{p}}n\Delta y) - 1] \\ & + A\sum_{m=0}^{M}\sum_{n=0}^{N}h_{mn}\frac{C_{mn}}{|\mathbf{x}_{mn}|^3}\boldsymbol{\Xi}_{mn}^{-}\hat{\mathbf{k}}[\cos(k_{\mathrm{x}}^{\mathrm{p}}m\Delta x - k_{\mathrm{y}}^{\mathrm{p}}n\Delta y) - 1] \\ & + B\sum_{m=0}^{M}\sum_{n=0}^{N}h_{mn}\frac{C_{mn}}{|\mathbf{x}_{mn}|^3}\boldsymbol{\Xi}_{mn}^{+}(\hat{\mathbf{z}}\times\hat{\mathbf{k}})[\cos(k_{\mathrm{x}}^{\mathrm{s}}m\Delta x + k_{\mathrm{x}}^{\mathrm{s}}n\Delta y) - 1] \\ & + B\sum_{m=0}^{M}\sum_{n=0}^{N}h_{mn}\frac{C_{mn}}{|\mathbf{x}_{mn}|^3}\boldsymbol{\Xi}_{mn}^{-}(\hat{\mathbf{z}}\times\hat{\mathbf{k}})[\cos(k_{\mathrm{x}}^{\mathrm{s}}m\Delta x - k_{\mathrm{x}}^{\mathrm{s}}n\Delta y) - 1], \end{aligned} \tag{22}$$

where

$$\boldsymbol{\Xi}_{mn}^{-} = \begin{bmatrix} m^2\Delta x^2 & -mn\Delta x\Delta y \\ -mn\Delta x\Delta y & n^2\Delta y^2 \end{bmatrix}, \tag{23}$$

$h_{mn} = 1 - \frac{1}{2}(\delta_m + \delta_n)$, and δ_m is the Kronecker delta function.

3 Implementation

Several implementation details are discussed in this section. First, the solution for the discrete micromodulus function coefficients is discussed in 1D, which simply requires the solution of a square system of equations. Second, the 2D implementation is detailed, which is complicated by a non-square system of equations. Finally, as mentioned above, the coefficients may be negative and result in instability when used with a standard bond-breakage scheme. Two methods of addressing this instability are discussed, a hybrid technique similar to that of hybrid finite difference and finite element schemes [33, 34] and an approach for constraining the coefficients.

3.1 1D Coefficient Solution

In 1D, the method is straightforward as a square system of equations can be formed at a given set of values of k and solved for the coefficients C_n. Thus, the only user-defined values for the 1D method are the choice of k at which the equations are enforced. The linear system then has the form

$$\mathbf{Ac} = \mathbf{b}, \tag{24}$$

where

$$\mathbf{A} = \begin{bmatrix} \cos(k_1\Delta x) - 1 & \frac{1}{2}(\cos(k_1 2\Delta x) - 1) & \dots & \frac{1}{N}(\cos(k_1 N\Delta x) - 1) \\ \vdots & \vdots & \ddots & \vdots \\ \cos(k_N\Delta x) - 1 & \frac{1}{2}(\cos(k_N 2\Delta x) - 1) & \dots & \frac{1}{N}(\cos(k_N N\Delta x) - 1) \end{bmatrix}, \tag{25}$$

and

$$\mathbf{b} = -\frac{\Delta x}{2}\begin{bmatrix} k_1^2 \\ \vdots \\ k_N^2 \end{bmatrix} \tag{26}$$

As an example, a set of micromodulus function coefficients was computed using $E = 1$ and $\rho = 1$, $\Delta t = 0.002$, $\Delta x = 0.01$, and $\delta = 3.5\Delta x$. If the spatial Nyquist sampling rate is given by $k_{\text{Nyq}} = \pi/\Delta x$, then choosing $k = \omega = k_{\text{Nyq}}[3 \times 10^{-5}\ 0.2\ 0.4] = [0.01\ 62.8\ 125.7]$ results in the coefficients

$$\mathbf{c} \approx [155.9\ \ -34.9\ 4.6]^{\text{T}}. \tag{27}$$

Clearly, (and unsurprisingly) the coefficients may be negative and the same will be true in 2D, leading to difficulties using standard bond-breakage schemes for damage modeling.

The above example used a linear dispersion relation, though the constant micromodulus function may be nearly recovered by using the dispersion relation of linearized peridynamics (with a constant micromodulus function) in 1D. In Eq. 12, the linear dispersion relation was substituted for ω, though if left unchanged, any arbitrary ω-k relation may be used. For example, setting $E = 1$ and $\rho = 1$, along with discretization parameters $\Delta t = 0.002$, $\Delta x = 0.01$, and $\delta = 3.5\Delta x$, the dispersion curve for linearized peridynamics with a constant micromodulus function is matched at the following points

$$\begin{aligned} k &= [100\ 150\ 200], \\ \omega &\approx [77.4\ 87.3\ 85.9], \end{aligned} \tag{28}$$

and results in the following coefficients

$$\mathbf{c} \approx [16.3\ 16.4\ 16.3]^{\text{T}}. \tag{29}$$

The 1D bond stiffness constant (multiplied by the node length) is

$$c\Delta x = \frac{2\Delta x E}{\rho\delta^2} \approx 16.3, \tag{30}$$

and thus the coefficients computed above closely match the linearized peridynamic bond stiffness. This suggests that other linear materials with dispersion may be treated with this technique, such as viscoelastic and periodic media.

3.2 2D Coefficient Solution

The main difficulty for the solution of the 2D system is that it may not be possible to form a square system of equations. Consider, the number of unknowns is $N_c = (N+1)^2 - 1$ (where $\delta = N\Delta x$) if the full quadrant is used or $N_c = (N+1)(N+2)/2 - 1$ for the unique unknowns. Figure 2 illustrates the unique coefficients in a square horizon for an isotropic material: Red nodes show the locations of the unique nodes, while light red nodes show their images across the $x = y$ line. Gray nodes indicate images across the $y = 0$ and $x = 0$ lines. On the other hand, the number of equations is given by $4N_\theta N_k$, where N_θ is the number of wave angles and N_k is the number of wavenumbers. The factor of 4 appears because there are two components of the displacement and two wave types (longitudinal and shear). The system may then be solved in a least-squares sense using the singular value decomposition.

The above method was applied with the following parameters: time step $\Delta t = 10$ ns, spatial intervals $\Delta x = \Delta y = 0.66667$ mm, Young's modulus 72 GPa, Poisson's ratio 0.25, density $\rho = 2440$ kg/m^3, and horizon $\delta = 3\Delta x$. The above equations were enforced at five frequencies linearly spaced between 10^{-8} Hz and 1 MHz (which represents 39% of the spatial Nyquist rate for the shear wave) and three angles $\theta = 0$, $\pi/4$, and $\pi/2$. Note that the system was constructed for all coefficients in the upper right quadrant, and symmetry across the $x = y$ line was enforced by using the angle $\theta = \pi/2$. This approach may result in a rank deficient system due to linear dependencies between the various components and directions, thus a larger than expected number of frequencies may be used. The coefficients resulting from the above parameters are then given in Table 1. Note that the coefficient 0.00

Table 1 Discrete micromodulus function coefficients (each normalized by 10^{14})

−0.34	0.35	−0.25	0.11
0.20	−0.53	0.31	−0.25
1.19	1.22	−0.53	0.35
0.00	1.19	0.20	−0.34

appearing in the bottom left is arbitrary as the peridynamic kernel is 0 at that point regardless.

For comparison, the constant micromodulus function (times the node volume with exact partial volumes at the cell-horizon intersections [22, 23]) for plane strain is shown in Table 2.

3.3 Stabilization

As expected, negative coefficients may result in unstable behavior when combined with a bond-breakage scheme. Two mitigation strategies are discussed here, though there may be alternative approaches that yield better results.

3.3.1 Positive Coefficients

One approach is to restate the coefficient solution as a constrained optimization problem wherein a positive lower bound is enforced on the coefficients. The optimization problem may be stated as

$$\begin{aligned} \min_{\mathbf{c}} \quad & \|\mathbf{Ac}-\mathbf{b}\|^2 \\ \text{subject to} \quad & l \le c_i,\ i=1,\ldots,N_c, \end{aligned} \tag{31}$$

where $l > 0$ is some positive lower bound. Of course, in terms of dispersion properties, coefficients computed using this approach will underperform those computed using an unconstrained method, though they should outperform standard peridynamics micromodulus functions. In addition, the dispersion characteristics of the coefficients will be highly dependent on the lower bound l.

To illustrate this method, the discrete micromodulus function coefficients were computed using the same parameters as given in Section 3.2, though now a lower bound of 10^{12} was used. The resulting coefficients are given in Table 3. Interestingly, the coefficients everywhere but near the origin are equal to the lower bound. This structure resembles the influence functions in Seleson and Parks [24] with high exponents that spike near the origin.

Coefficients were also computed for varying lower bounds, and the structure of the solution is identical to that in Table 3: Aside from the three coefficients neighboring the origin, all coefficients are equal to the lower bound l. Further, these three coefficients asymptote to a given value as the lower bound decreases, as shown in Fig. 3. In Fig. 3, the coefficients were computed using the constrained method for varying lower bound l, from 10^{12} to 10^2, and the two unique coefficients are shown. As the lower bound decreases, the method begins to resemble a local method (with improved dispersion properties) and thus we anticipate that the fracture solutions will suffer as a result. In general, we find that using a lower bound of about 1 order of magnitude lower than the bond stiffness for a constant influence function provides a reasonable trade-off.

Table 2 Constant micromodulus function with partial area (each normalized by 10^{13})

0.59	0.38	0.01	0.00
1.22	1.22	0.85	0.01
1.22	1.22	1.22	0.38
1.22	1.22	1.22	0.59

Table 3 Discrete micromodulus function constrained solution (each normalized by 10^{13})

0.10	0.10	0.10	0.10
0.10	0.10	0.10	0.10
7.57	5.08	0.10	0.10
0.00	7.57	0.10	0.10

3.3.2 Hybridized Method

Similar to the technique used in Wildman and Gazonas [33] and Wildman et al. [34], a hybrid approach may also be used. With this approach, the more accurate, discrete micromodulus function is used while no damage has occurred and after damage initiates at a node, the micromodulus function is replaced with a standard peridynamics micromodulus function. In other words, two

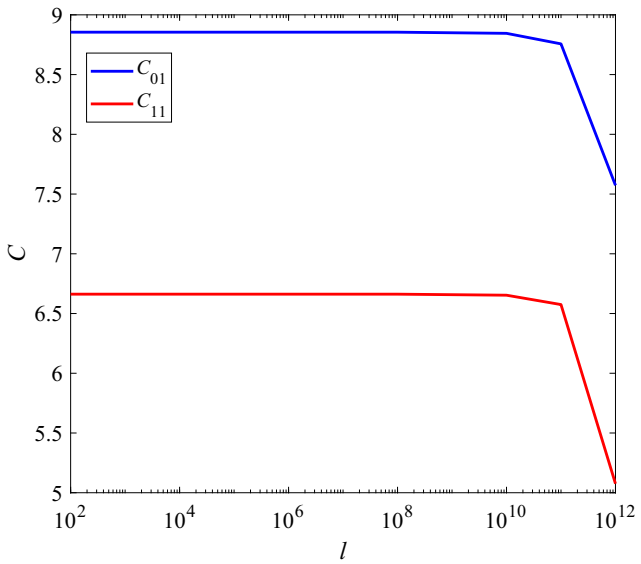

Fig. 3 Neighboring coefficient values (normalized by 10^{13}) versus lower bound for the constrained coefficient solution

sets of micromodulus function coefficients are used to compute the force at a node, according to

$$\mathbf{f}_i = \begin{cases} \sum_j c_{ij}^{\text{dmm}} \dfrac{\boldsymbol{\xi}_{ij} \otimes \boldsymbol{\xi}_{ij}}{|\boldsymbol{\xi}_{ij}|^3} \boldsymbol{\eta}_{ij} & \text{if } \chi(t,\boldsymbol{\xi}) = 1 \text{ for all } \mathbf{x}' \in \mathcal{H} \\ \sum_j \chi c_{ij}^{\text{pd}} \dfrac{\boldsymbol{\xi}_{ij} \otimes \boldsymbol{\xi}_{ij}}{|\boldsymbol{\xi}_{ij}|^3} \boldsymbol{\eta}_{ij} & \text{otherwise} \end{cases}, \tag{32}$$

where c_{ij}^{dmm} are the coefficients of the discrete micromodulus function, c_{ij}^{pd} are the coefficients of peridynamics with a constant micromodulus function (times the nodal volume), and χ is the bond health given by

$$\chi(t,\boldsymbol{\xi}) = \begin{cases} 1 & \text{if } s(t',\boldsymbol{\xi}) < s_0 \text{ for all } 0 < t' < t \\ 0 & \text{otherwise} \end{cases}, \tag{33}$$

where s_0 is the critical bond stretch which may be related to energy release rate or fracture toughness [12, 27]. For the discrete micromodulus functions (and assuming that the node area is accounted for in the micromodulus function coefficients), the critical stretch may be related to the energy release rate G_0 as

$$s_0^2 = \frac{2G_0}{\sum_{l=0}^{N} \sum_{m=-M}^{M} \sum_{n=l}^{N} \Delta y c_{mn} |\boldsymbol{\xi}_{mn}|}, \tag{34}$$

which is a discretized form of the critical stretch relations in Silling and Askari [27] and Ha and Bobaru [12] for rectangular horizons.

4 Dispersion Comparison

In this section, the dispersion characteristics of the various micromodulus functions are compared. First, the 1D approach is compared with linearized peridynamics using a constant micromodulus function along with various finite difference stencils. Second, both the constrained and unconstrained 2D methods are compared with linearized peridynamics with a constant micromodulus function and the numerical anisotropy is illustrated.

4.1 1D

The dispersion relations for the discretized methods may be computed in 1D following the formulation given in Section 2.1 with the only difference being the discretization of time. For the linearized, spatially discretized peridynamic equation of motion with arbitrary coefficients in 1D and a second-order finite difference method in time, the dispersion relation can be shown to be

$$\cos(\Delta t \omega) = \Delta t^2 \sum_{n=1}^{N} \frac{C_n}{n\Delta x} [\cos(nk\Delta x) - 1] + 1. \tag{35}$$

In 1D, the constant micromodulus function coefficients are equal to the peridynamic constant given in Eq. 30, and for the proposed discrete micromodulus function method, they are computed as described in Section 3.1.

Figure 4 gives a comparison of the dispersion curves associated with a constant micromodulus function (CMM) and the discrete micromodulus (DMM) function using a wavespeed of 1 and temporal discretization $\Delta t = 0.002$, spatial discretization $\Delta x = 0.01$, and horizon size $\delta = 3\Delta x$ giving $N = 3$. Further, the dispersion curve for a second-order finite difference method is shown for reference. As can be seen, the discrete micromodulus function matches the exact linear dispersion closely even to high frequencies, while the constant micromodulus function dispersion curve flattens out. This result is of course not surprising as this behavior was designed into the method. More interesting is that the discrete micromodulus function yields a discretization that is more accurate than a second-order finite difference method.

A more fair comparison would be against higher order finite difference methods, which use additional degrees of freedom to more accurately approximate the spatial derivatives. For example, a fourth-order accurate central difference method uses five discretization points and a sixth-order accurate method uses seven points, which corresponds to $N = 3$. The relative error (compared with the exact, linear dispersion) in the dispersion curve for the

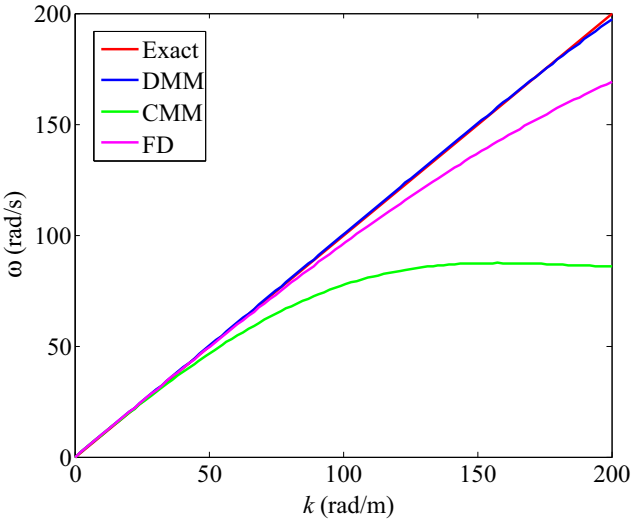

Fig. 4 Comparison of dispersion curves for the exact solution (red), constant micromodulus function (green), finite difference method (magenta), and the discrete micromodulus function (blue)

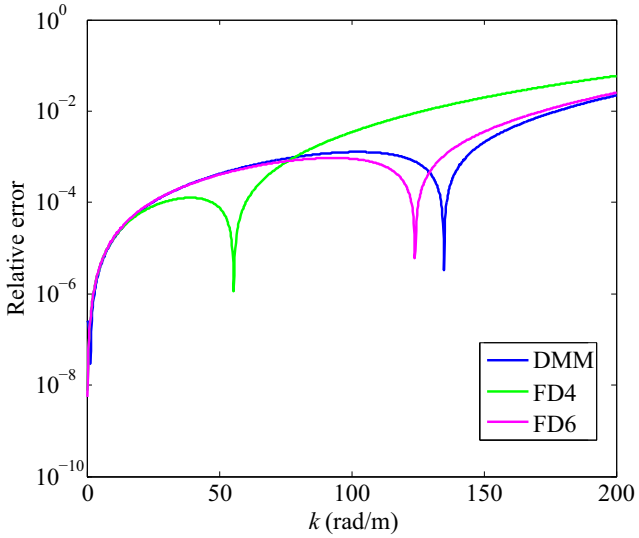

Fig. 5 Relative error of dispersion curves for the discrete micromodulus function (blue), a fourth-order central difference method (green), and a sixth order central difference method (magenta)

discrete micromodulus function method was then compared with that of the fourth- and sixth-order central difference methods and is shown in Fig. 5. As can be seen, the discrete micromodulus function compares well with the sixth-order finite difference method.

4.2 2D

Similar to the 1D case, the dispersion curves can be calculated in 2D. Again assuming a second-order explicit method in time, the 2D dispersion relation can be written as

$$\begin{aligned}
&\Delta t^{-2}[A\hat{\mathbf{k}} + B(\hat{\mathbf{z}} \times \hat{\mathbf{k}})][\cos(\Delta t\omega) - 1] \\
&\quad = A \sum_{m=0}^{M} \sum_{n=0}^{N} h_{mn} \frac{C_{mn}}{|\mathbf{x}_{mn}|^3} \boldsymbol{\Xi}^{+}_{mn} \hat{\mathbf{k}} [\cos(k^{\mathrm{p}}_{\mathrm{x}} m\Delta x + k^{\mathrm{p}}_{\mathrm{y}} n\Delta y) - 1] \\
&\quad + A \sum_{m=0}^{M} \sum_{n=0}^{N} h_{mn} \frac{C_{mn}}{|\mathbf{x}_{mn}|^3} \boldsymbol{\Xi}^{-}_{mn} \hat{\mathbf{k}} [\cos(k^{\mathrm{p}}_{\mathrm{x}} m\Delta x - k^{\mathrm{p}}_{\mathrm{y}} n\Delta y) - 1] \\
&\quad + B \sum_{m=0}^{M} \sum_{n=0}^{N} h_{mn} \frac{C_{mn}}{|\mathbf{x}_{mn}|^3} \boldsymbol{\Xi}^{+}_{mn} (\hat{\mathbf{z}} \times \hat{\mathbf{k}}) \\
&\quad \times [\cos(k^{\mathrm{s}}_{\mathrm{x}} m\Delta x + k^{\mathrm{s}}_{\mathrm{x}} n\Delta y) - 1] \\
&\quad + B \sum_{m=0}^{M} \sum_{n=0}^{N} h_{mn} \frac{C_{mn}}{|\mathbf{x}_{mn}|^3} \boldsymbol{\Xi}^{-}_{mn} (\hat{\mathbf{z}} \times \hat{\mathbf{k}}) \\
&\quad \times [\cos(k^{\mathrm{s}}_{\mathrm{x}} m\Delta x - k^{\mathrm{s}}_{\mathrm{x}} n\Delta y) - 1]. \qquad (36)
\end{aligned}$$

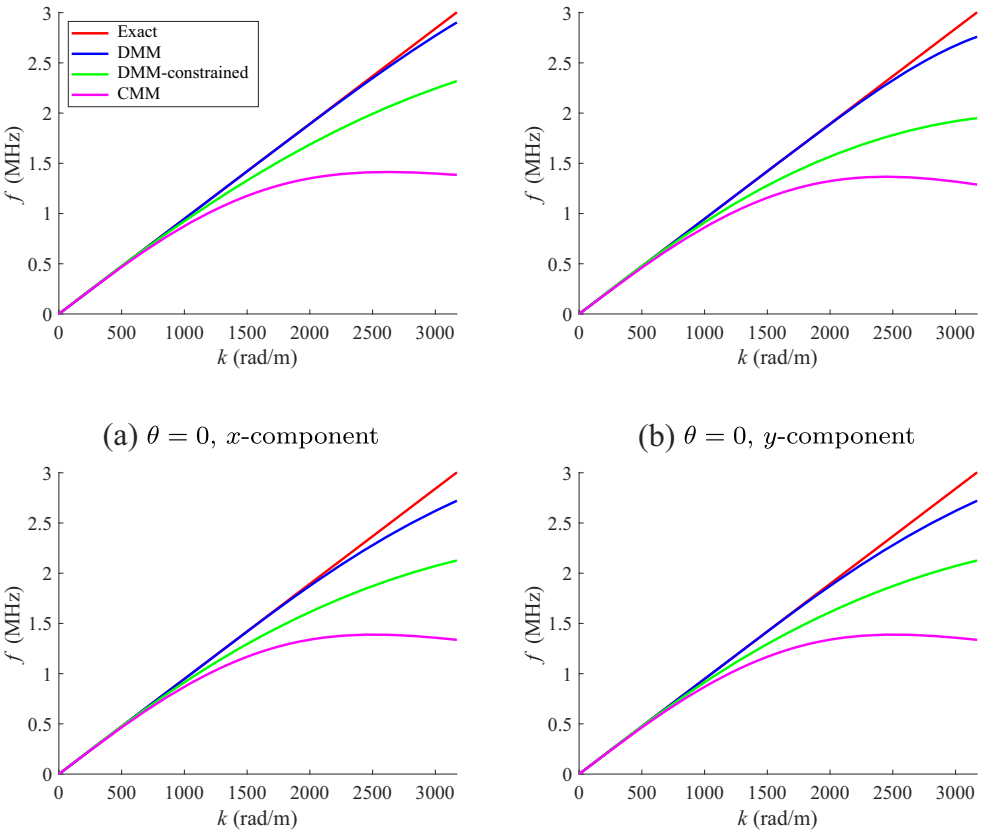

(a) $\theta = 0$, x-component (b) $\theta = 0$, y-component

(c) $\theta = \pi/4$, x-component (d) $\theta = \pi/4$, y-component

Fig. 6 Comparison of p-wave dispersion curves for the exact solution (red), constant micromodulus function (magenta), the discrete micromodulus function (blue), and a constrained solution (green)

In this case, the dispersion curves may be separated by displacement component (x- and y-components) and wave type (p- and s-waves). Further, the dispersion relation is a function of both wavenumber k and wave direction θ and may be visualized by fixing either. Fixing the angle and varying k results in a dispersion curve similar to the 1D case, while fixing k (or frequency f) and varying the angle, illustrates the numerical anisotropy in the method.

The dispersion in linearized peridynamics using a constant micromodulus function is compared with both the unconstrained and constrained solution approaches in Fig. 6 for the p-wave and in Fig. 7 for the s-wave. Figure 6a shows the dispersion in the x-component of displacement at $\theta = 0$ for the exact solution (red), constant micromodulus function (magenta), the unconstrained coefficients (blue), and the constrained coefficients (green). The y-component of displacement is shown in Fig. 6b and the x- and y-components at 45° are shown in Fig. 6c and d respectively. The same results are given for the s-wave in Fig. 7. As with the 1D case, the 2D formulation exhibits improved dispersion characteristics when compared with the exact local dispersion.

Finally, the numerical anisotropy of the various methods is compared by plotting the phase velocity at a given frequency over all wave directions. Specifically, Figs. 8 and 9 illustrate the phase velocity vs. angle for the constant micromodulus function and both the constrained and unconstrained solutions of the discrete micromodulus function. Specifically, Fig. 8a and b shows the phase velocity of the x- and y-components of the p-wave at 150 kHz respectively and Fig. 8c and d shows the phase velocity at 1.5 MHz. Similar results are shown for the s-wave in Fig. 9. As before, these figures demonstrate the frequency-dependent nature of the phase velocity and further illustrate anisotropic wave propagation at high frequencies.

5 Results

Several numerical examples are given in this section, beginning with 1D wave propagation. Next, 2D wave propagation is demonstrated and comparisons are made between the various micromodulus functions. Finally, the

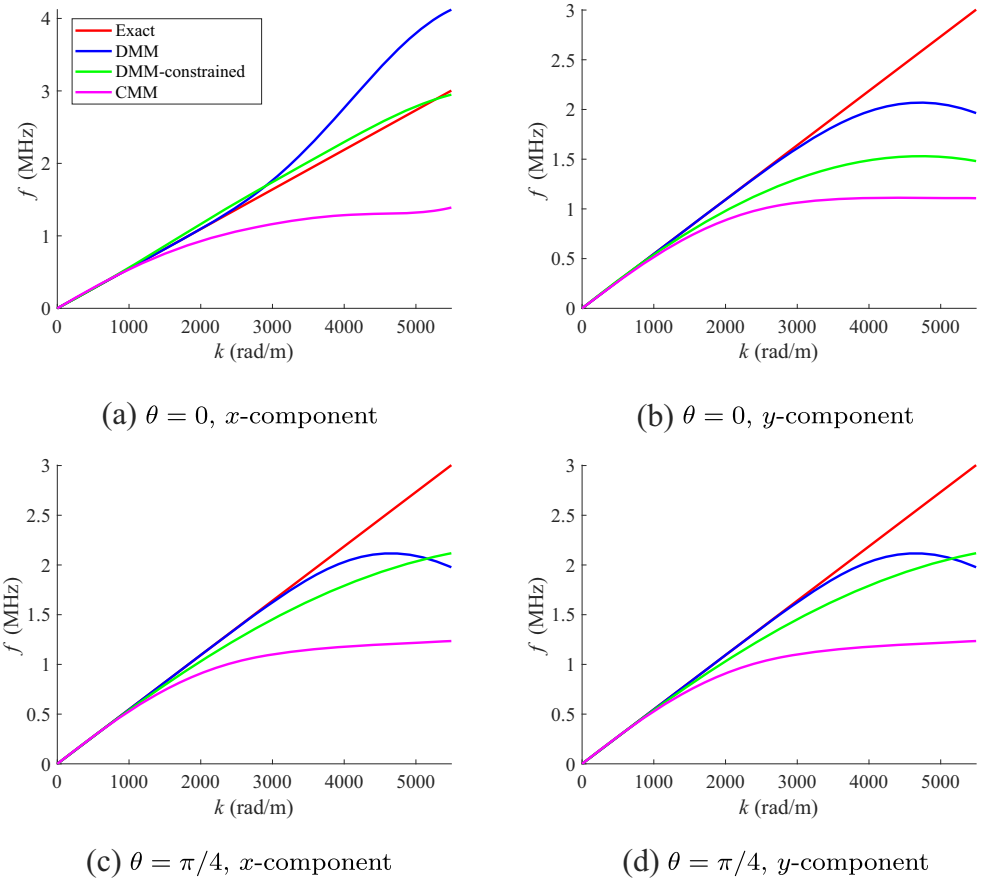

Fig. 7 Comparison of s-wave dispersion curves for the exact solution (red), constant micromodulus function (magenta), the discrete micromodulus function (blue), and a constrained solution (green)

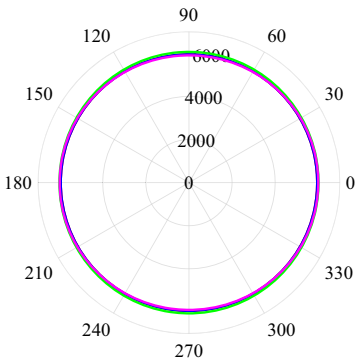

(a) $f = 150$ kHz, x-component

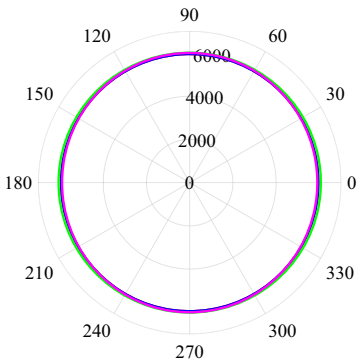

(b) $f = 150$ kHz, y-component

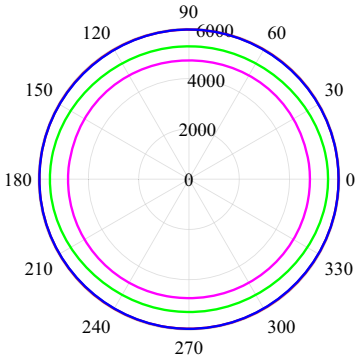

(c) $f = 1.5$ MHz, x-component

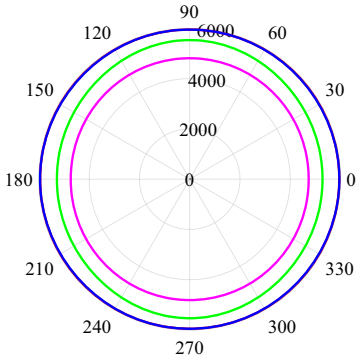

(d) $f = 1.5$ MHz, y-component

Fig. 8 Comparison of p-wave numerical anisotropy for the exact solution (red), constant micromodulus function (magenta), the discrete micromodulus function (blue), and the constrained solution (green)

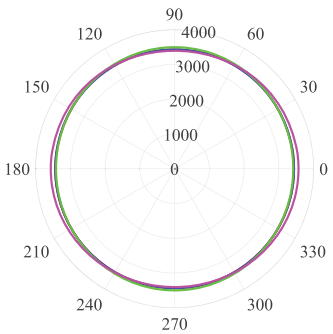

(a) $f = 150$ kHz, x-component

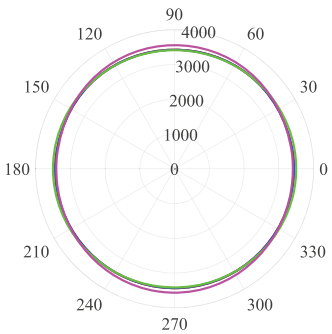

(b) $f = 150$ kHz, y-component

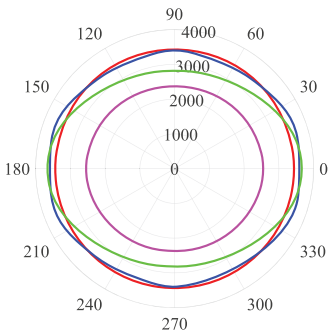

(c) $f = 1.5$ MHz, x-component

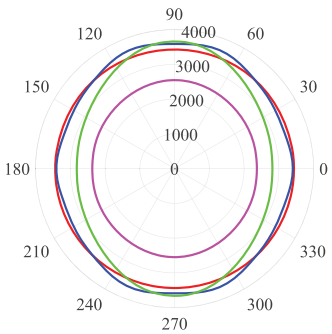

(d) $f = 1.5$ MHz, y-component

Fig. 9 Comparison of s-wave numerical anisotropy for the exact solution (red), constant micromodulus function (magenta), the discrete micromodulus function (blue), and the constrained solution (green)

stress intensity factor is computed and compared and results of several dynamic fracture tests are given to illustrate the stabilization techniques.

5.1 1D Wave Propagation

To demonstrate the discrete micromodulus function in 1D, the coefficients given in Section 3.1 were used to simulate propagation of a Gaussian initial condition given by

$$u = e^{-\alpha x^2}, \tag{37}$$

where $\alpha = 200$. The simulation region was 2 m in length and both Dirichlet and Neumann boundary conditions were tested. The wave speed and region size are such that the pulse should, after reflection from the boundaries, return to the origin at $t = 2$. First, Fig. 10 shows the displacement computed using the discrete micromodulus function and a constant micromodulus function at four instances of time. The effects of dispersion are apparent for the constant micromodulus function as the wave is slow to arrive at the origin at $t = 2$ and spurious oscillations are visible. In contrast, the discrete micromodulus function more accurately captures the correct wave velocity over the range of frequencies present in this initial condition.

Second, the simulation was repeated with Neumann boundary conditions as shown in Fig. 11. These results are similar to the results using Dirichlet boundary conditions in that the constant micromodulus function exhibits significant dispersion, while the discrete micromodulus function appears more accurate.

5.2 2D Wave Propagation

The 2D micromodulus functions were tested by inducing 1D-like wave propagation of the p- and s-waves in large regions at two different angles. The initial conditions used here are given by

$$\mathbf{u}_\mathrm{p} = A\hat{\mathbf{n}} e^{-\alpha[(\mathbf{x}-\mathbf{x}_\mathrm{c})\cdot\hat{\mathbf{n}}]^2}, \tag{38}$$

and

$$\mathbf{u}_\mathrm{s} = A(\hat{\mathbf{z}}\times\hat{\mathbf{n}}) e^{-\alpha[(\mathbf{x}-\mathbf{x}_\mathrm{c})\cdot\hat{\mathbf{n}}]^2}, \tag{39}$$

where $A = 10^{-8}$, $\alpha = 10^5$, $\mathbf{x}_\mathrm{c}$ is the center location of the initial condition, and $\hat{\mathbf{n}} = [\cos\phi, \sin\phi]^\mathrm{T}$ indicates the propagation direction. Further, $\mathbf{u}_\mathrm{p}$ will induce a compressional wave and $\mathbf{u}_\mathrm{s}$ will induce a shear wave.

First, propagation along $\phi = 0$ was simulated using the same parameters as given in Section 3.2 using a constant micromodulus function, an unconstrained discrete

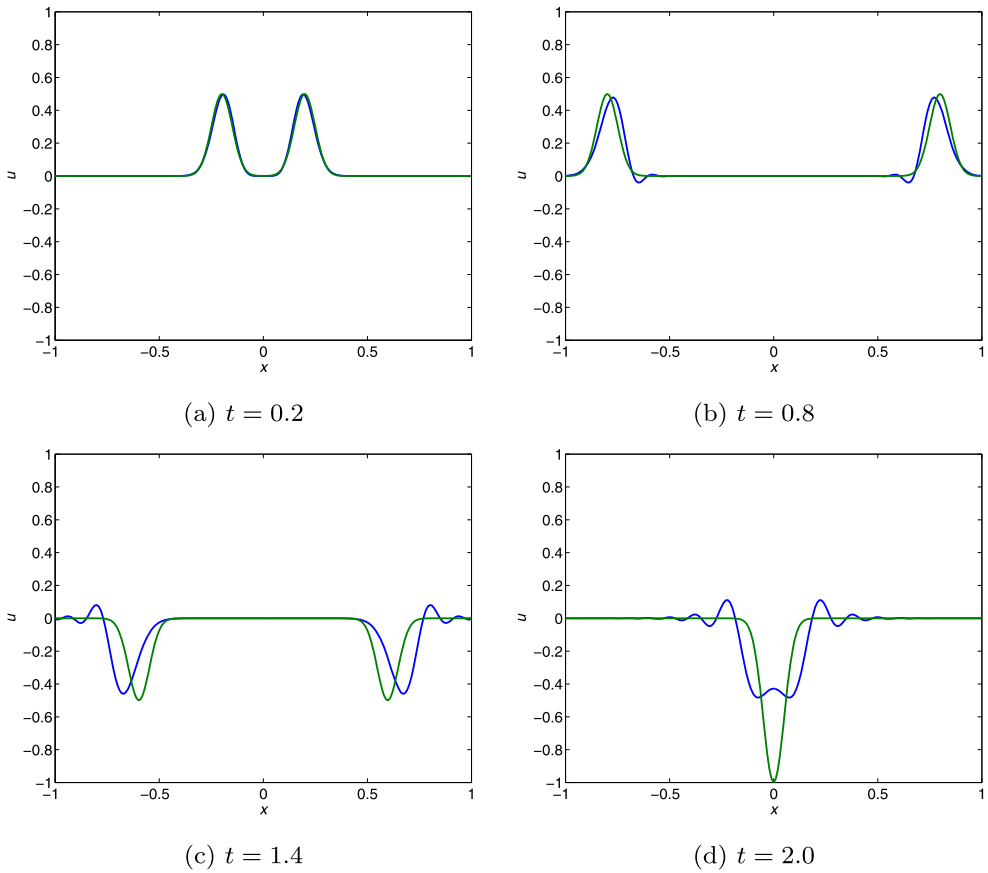

(a) $t = 0.2$ (b) $t = 0.8$

(c) $t = 1.4$ (d) $t = 2.0$

Fig. 10 1D wave propagation using linearized peridynamics with a constant micromodulus function (blue) and the discrete micromodulus function (green) with Dirichlet boundary conditions

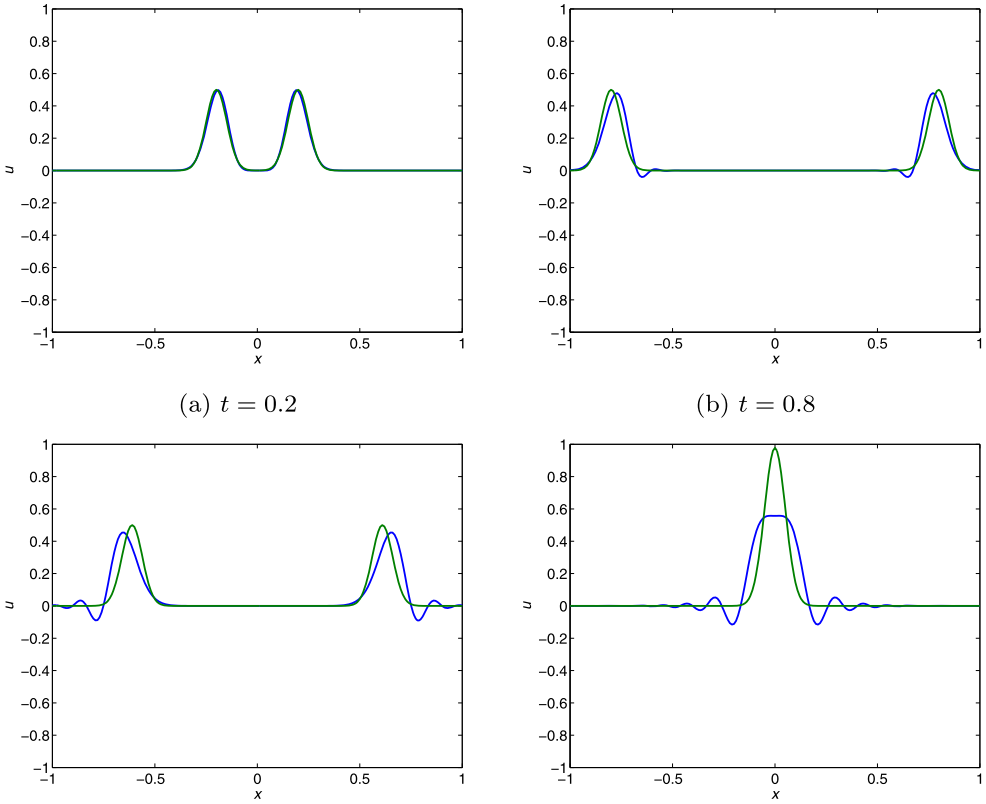

Fig. 11 1D wave propagation using linearized peridynamics with a constant micromodulus function (blue) and the discrete micromodulus function (green) with Neumann boundary conditions

micromodulus function, and a constrained micromodulus function each assuming plane strain. The coefficients for each are given in Tables 1, 2, and 3. The region was 100-by-200 mm with the initial condition placed at the point $\mathbf{x}_c$ = (50 mm, 100 mm). Figure 12 shows the x-component of displacement using the initial condition given in Eq. 38 at three locations along the y = 50 mm line (x = 10, 20 and 30 mm) versus time for each method. Specifically, the results using the constant micromodulus function are shown in blue with the solid line showing the displacement at 30 mm, the dashed line showing the displacement at 20 mm, and the dotted line representing 10 mm. Similarly, the displacements for the unconstrained discrete micromodulus function are shown in red and for the constrained discrete micromodulus function in green. Dispersion effects are clearly visible in both the constant micromodulus function and to a lesser extent the constrained micromodulus function. To quantify these effects, the wave speed may be estimated for each method by tracking the propagation of the initial condition through the region. To estimate the wave speed, at each location, the propagation time to that point was taken to be coincident with the maximum of the displacement. The resulting wave speed estimates are given in Table 4 and the exact wave speed is 5950.62 m/s.

Figure 13 illustrates the propagation of the initial condition given in Eq. 39, representing propagation of a shear wave. The colors and line styles in the figure are the

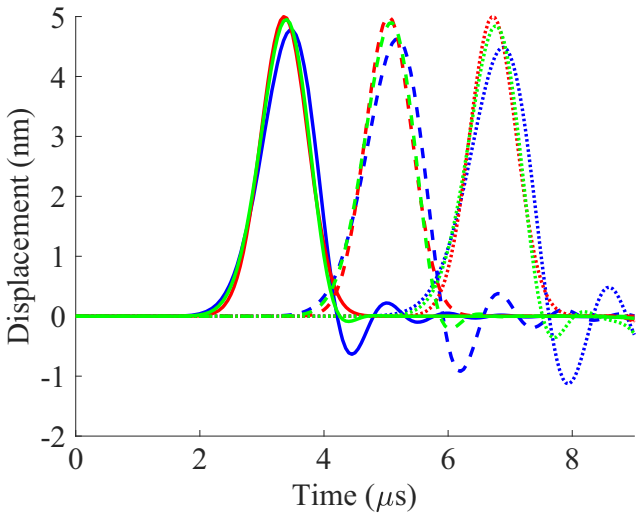

Fig. 12 x-directed displacement (p-wave) at three points (x = 10, 20, and 30 mm) in a 2D simulation for a constant micromodulus function (blue), unconstrained discrete micromodulus function (red), and constrained discrete micromodulus function (green)

Table 4 Estimated longitudinal wave speeds (in m/s) from Fig. 12

	CMM	DMM	DMM-constrained
$x = 10$ mm	5811	5951	5909
$x = 20$ mm	5790	5951	5904
$x = 30$ mm	5764	5951	5899

Table 5 Estimated shear wave speeds (in m/s) from Fig. 13

	CMM	DMM	DMM-constrained
$x = 10$ mm	3330	3435	3439
$x = 20$ mm	3331	3436	3443
$x = 30$ mm	3321	3436	3440

same as the above example. Again, the shear wave speed can be estimated from these results as given in Table 5, and the exact shear wave speed is 3435.59 m/s.

The same tests were repeated using an initial condition with $\phi = \pi/4$ and a region size of 200-by-200 mm with the p-wave results shown in Fig. 14 (i.e., the initial condition is that of Eq. 38) and the s-wave results are shown in Fig. 15. In each figure, the magnitude of the displacement is shown, again with the same colors and line styles as before, though now the displacement is shown at the points (114, 114), (121.333, 121.333), and (128, 128) (all in mm).

As before, the wave speeds were estimated at each point and can be compared with the exact wave speeds for both longitudinal and shear waves. Table 6 lists the estimated wave speeds for the longitudinal wave and Table 7 lists the estimated wave speeds for the shear wave. The results are similar to the above example (with $\phi = 0$) in that the unconstrained discrete micromodulus function exhibits minimal dispersion for this initial condition, while the constant micromodulus function exhibits visible dispersion in terms of a slower wave speed, spurious oscillations, and amplitude reduction.

5.3 Static Fracture

As described in Wildman and Gazonas [33], the dynamic mode I stress intensity factor at a static crack tip can be computed and used to compare the methods. For a semi-infinite crack, the stress intensity factor is given as

$$K_{\mathrm{I}}(t) = H(t - t_{\mathrm{c}}) \frac{2\sigma^*}{1-\nu} \sqrt{\frac{v_{\mathrm{l}}(t - t_{\mathrm{c}})(1-2\nu)}{\pi}}, \tag{40}$$

where v_{l} is the longitudinal wave speed, t_{c} is the time for the initial stress wave to reach the crack tip, and σ^* is the applied stress [18]. For the numerical solution to this problem, a large region can be used to approximate a semi-infinite crack in an infinite medium. The stress intensity

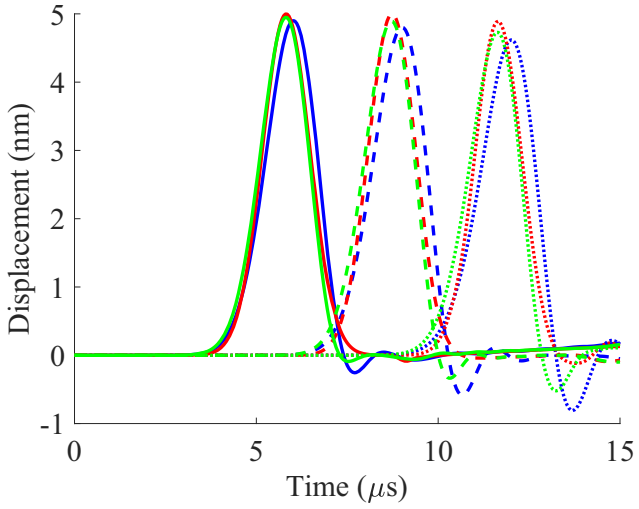

Fig. 13 y-directed displacement (s-wave) at three points ($x = 10$, 20, and 30 mm) in a 2D simulation for a constant micromodulus function (blue), unconstrained discrete micromodulus function (red), and constrained discrete micromodulus function (green)

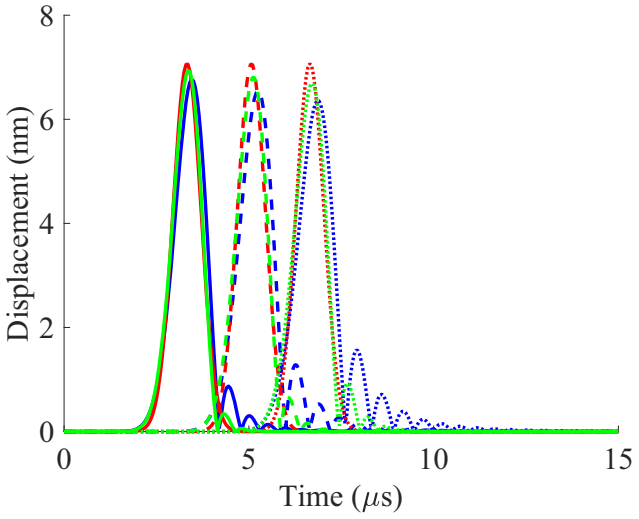

Fig. 14 Displacement magnitude (p-wave) at three points ($x = y = 114$, 121.333, and 128 mm) in a 2D simulation for a constant micromodulus function (blue), unconstrained discrete micromodulus function (red), and constrained discrete micromodulus function (green)

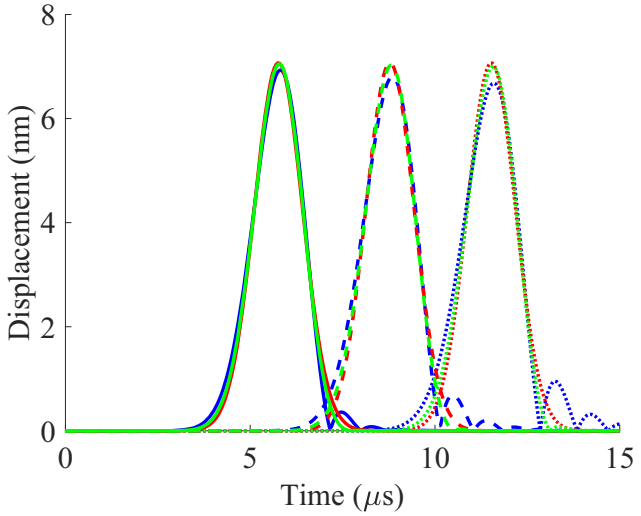

Fig. 15 Displacement magnitude (s-wave) at three points ($x = 10$, 20, and 30 mm) in a 2D simulation for a constant micromodulus function (blue), unconstrained discrete micromodulus function (red), and constrained discrete micromodulus function (green)

factor can then be approximated by first computing the stress along a straight line near the crack and extrapolating the stress towards the crack tip. The extrapolated value of the stress can be then used to approximate the stress intensity factor [5]. As shown in Chen [5], all components of the stress may be used to approximate the stress intensity factor, and so here both σ_{xx} and σ_{yy} are used and the results are averaged. Since a Cartesian grid is used, the stress is computed by first computing the local strain using a standard finite difference approximation and the local linear elastic constitutive relation was then used to compute the stress.

The stress intensity factor for a semi-infinite crack was then estimated using a 300 mm-by-100 mm region with the same material properties and discretization as used above. The force was applied using a body force with a magnitude of 10^{10}, and according to Ha and Bobaru [11], the equivalent traction is $\mathbf{t} = \mathbf{b}/\Delta x$, giving $|\mathbf{t}| = \sigma^* = 6.66667$ MPa. Further, the coefficients of the micromodulus functions were those given by Tables 1, 2, and 3. The results are given in Fig. 16, where the red curve represents the exact solution,

Table 6 Estimated longitudinal wave speeds (in m/s) from Fig. 14

	CMM	DMM	DMM-constrained
$x = y = 128$ mm	5766	5951	5899
$x = y = 121.33$ mm	5747	5951	5890
$x = y = 114$ mm	5721	5951	5879

Table 7 Estimated shear wave speeds (in m/s) from Fig. 15

	CMM	DMM	DMM-constrained
$x = y = 128$ mm	3415	3436	3422
$x = y = 121.33$ mm	3410	3436	3422
$x = y = 114$ mm	3403	3436	3421

peridynamics with a constant micromodulus function is shown in blue, the unconstrained micromodulus function is shown in green, and the constrained micromodulus function is shown in yellow. Note that the discrete micromodulus function is not the hybrid form described in Eq. 32, and only uses the discrete micromodulus function. Similar to the results in Wildman and Gazonas [33], these results illustrate that the constant micromodulus function displays spurious oscillations that may affect crack propagation paths. Both discrete micromodulus functions reduce the spurious oscillations seen in the solution, especially at longer times.

5.4 Dynamic Fracture

To demonstrate dynamic fracture, two examples from Kalthoff [17] were attempted using the standard constant micromodulus function, the unconstrained method (using the hybrid technique described in Section 3.3.2), and the constrained method. The material properties and discretization parameters were identical to those given in Section 3.2 and the critical bond stretch criterion was $s_0 =$

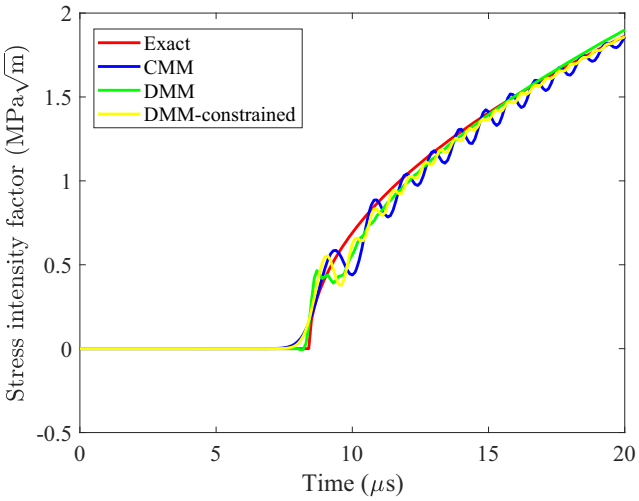

Fig. 16 Stress intensity factor comparison using a constant micromodulus function, and unconstrained and constrained discrete micromodulus functions

Fig. 17 Damage at 100 μs

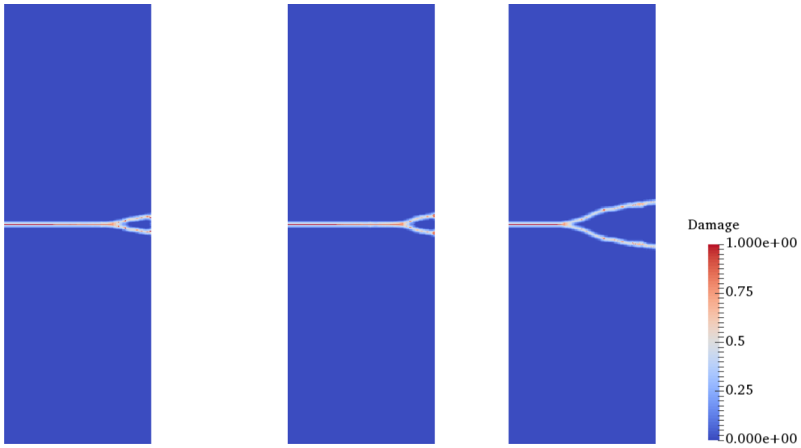

(a) Constant micromodulus function (b) Hybrid unconstrained approach (c) Constrained approach.

3.69×10^{-4}. (Note that expressions from e.g. Silling and Askari [27] relating energy release rate and critical stretch do not apply and must be recomputed for the discrete micromodulus functions.)

The first example is a 100-by-300 mm plate with a 33-mm pre-notch subjected to sudden tension along the top and bottom edges. The load was a body force applied to the nodes on the top and bottom edges, with a magnitude of 5.0685×10^9 N/m^3 (or 310 kp [17]). Figure 17 shows the peridynamic damage (ratio of the number of broken bonds to unbroken bonds in a node's horizon) at 100 μs. The results compare well with the experimental results in Kalthoff [17]. While the constrained micromodulus function branches earlier than the other two approaches, the branch in the experimental results was estimated to occur at the midpoint (50 mm). The crack branch for the result obtained using the constrained coefficients occurs at approximately 42 mm, and the branch in the constant micromodulus function and hybrid results occurs at approximately 81 mm. The results using the constrained coefficients appear to be closer to the experiment, though it is difficult to make a quantitative assessment because the length of the pre-notch and the material properties are not known for the experiment.

For reference, Fig. 18 illustrates the instability seen for negative coefficients in the micromodulus function. The same loading was used as above, though here no hybrid approach was used. Figure 18 shows the damage at 55, 60, and 65 μs and demonstrates unstable growth of damage.

The final example follows the test in Kalthoff [17] in which crack propagation from branched edge notches at different angles are compared. It was shown that a critical angle exists (approximately 16°) at which cracks propagating from a branched edge notch will either converge towards or diverge from the centerline immediately at the onset of crack propagation. (Note that

Fig. 18 Unstable damage for negative coefficients

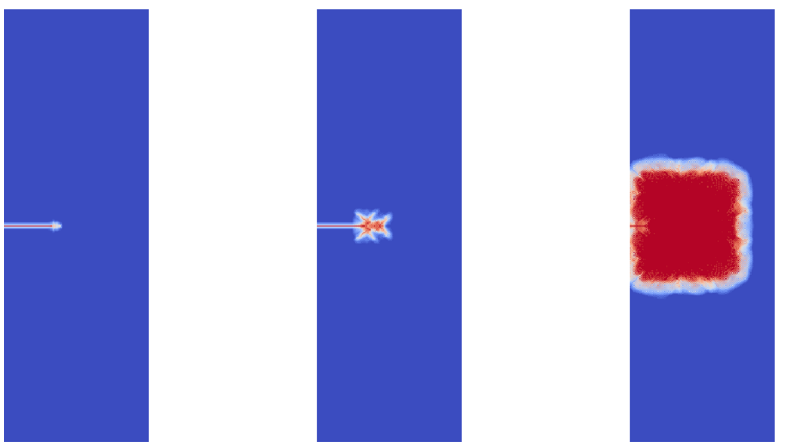

(a) Damage at 55 μs (b) Damage at 60 μs (c) Damage at 65 μs

after crack propagation continues, the crack path is less dependent on the initial pre-notch.) The three approaches were tested on the four examples in Kalthoff [17], which consist of branched edge notches of 5.7°, 11.3°, 16.7°, and 21.8°. In this case, the plate size was 120-by-260 mm and the pre-notches were an equal depth of 43 mm. For each example, the critical stretch was $s_0 = 3 \times 10^{-4}$, and all other properties were identical to those used in the previous example.

Figures 19, 20, and 21 show the peridynamic damage at 150 μs for each edge notch angle using the three methods. The main comparison to consider is the crack angle relative to the pre-notch immediately after propagation begins. For edge notches with angles below 16°, the crack should propagate away from the centerline and for edge notches with angles above 16° the crack should propagate towards the centerline relative to the edge notch [17]. Computing this angle quantitatively is difficult with peridynamics as there is no discrete fracture surface, so a qualitative comparison will be made. The constant micromodulus function and hybrid unconstrained discrete micromodulus function methods appear to give similar results in that the initial crack path appears to be away from the center for 5.7° edge notch and towards the center for the remaining examples. This result appears to be at odds with the experimental and analytical results in Kalthoff [17]. However, the constrained discrete micromodulus function appears to be correct: The initial crack path is angled away from the center for both the 5.7° and 11.3° edge notches and towards the center for the remaining two examples. This indicates that the state of stress around the crack tip may be more accurate for the constrained micromodulus function.

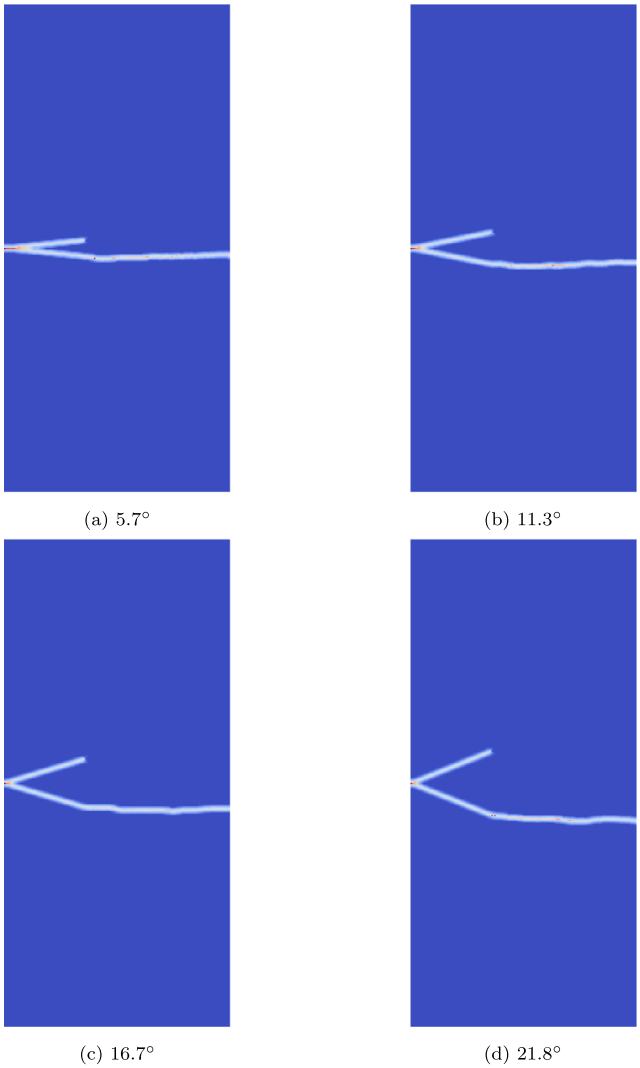

(a) 5.7° (b) 11.3° (c) 16.7° (d) 21.8°

Fig. 19 Damage at 150 μs for the branched edge notch using the constant micromodulus function

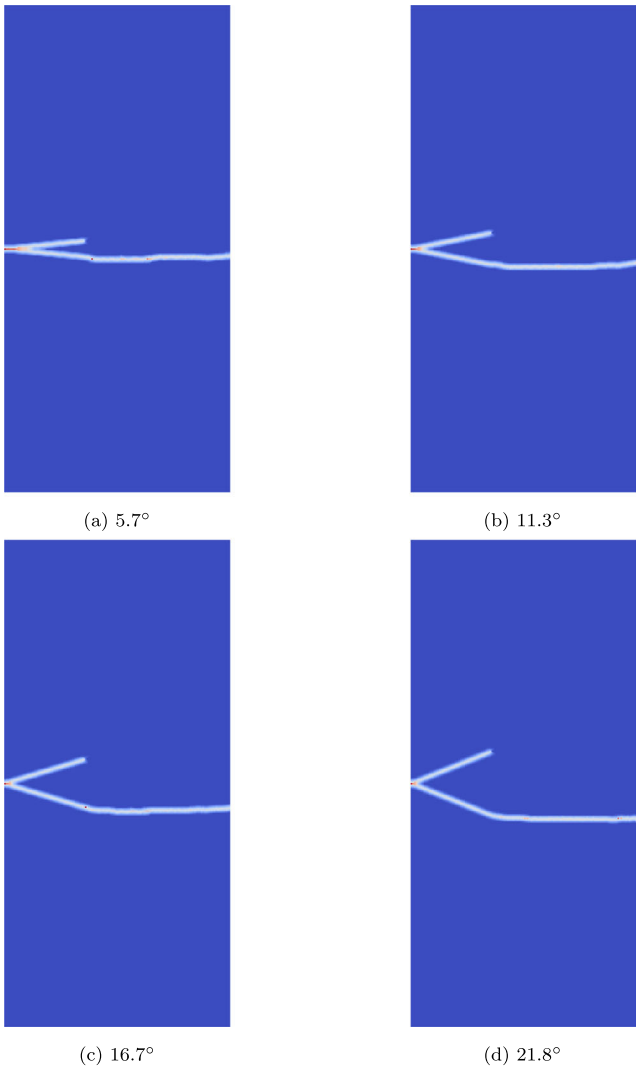

(a) 5.7° (b) 11.3° (c) 16.7° (d) 21.8°

Fig. 20 Damage at 150 μs for the branched edge notch using the hybrid unconstrained discrete micromodulus function

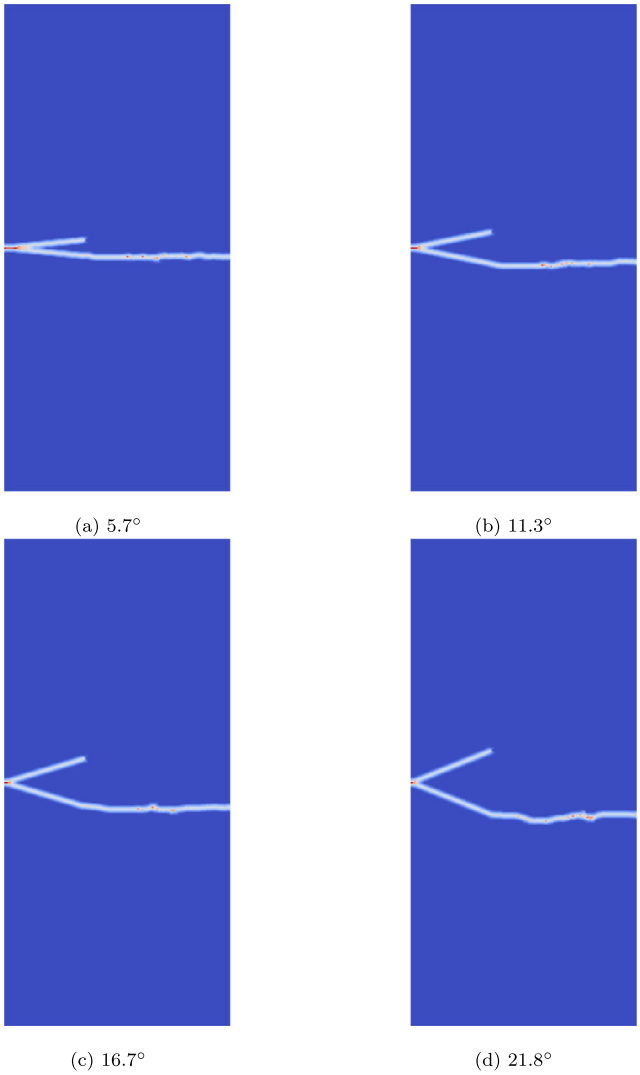

Fig. 21 Damage at 150 μs for the branched edge notch using the constrained discrete micromodulus function

6 Conclusions

A method for reducing wave dispersion in linearized peridynamics was presented, which computes values of a micromodulus function at discrete points to match a given dispersion curve. Linear dispersion curves were treated, though it was shown that a near-constant micromodulus function can be recovered if ω-k pairs from a standard, linear peridynamics formulation are used. The method results in micromodulus function values that can be negative and resemble high-order finite difference schemes, making them difficult to use directly in a dynamic fracture simulation. Two approaches for stabilizing the scheme were discussed, the first being a hybrid discrete/constant micromodulus function method and the second using constrained optimization to ensure only positive coefficients constitute the micromodulus function. The resulting numerical dispersion relations were studied in 1D and 2D and in 2D, the numerical anisotropy was also computed. Plots of the dispersion relations show that the discrete micromodulus functions are more accurate versus a constant micromodulus function at higher frequencies. Numerical results also show the efficacy of the method: 1D and 2D wave propagation simulations are more accurate and mitigate the effects of numerical dispersion such as spurious oscillations. The stress intensity factor around a crack tip was also shown to be more accurate and smooth than that computed using a constant micromodulus function. Finally, dynamic fracture simulations using the two stabilization techniques show stable crack propagation, and the constrained micromodulus function shows improved crack path accuracy for a branched edge notch problem.

While the method was formulated in 2D, an extension to 3D is straightforward, if somewhat involved due to the additional wave components. In addition, dispersive materials could be treated with this approach including periodic materials and possibly viscoelastic. Finally, linearized bond-based peridynamics was the basis of the formulation, though the method could also be applied to linearized state-based peridynamics.

References

1. Azdoud Y, Han F, Lubineau G (2014) The morphing method as a flexible tool for adaptive local/non-local simulation of static fracture. Comput Mech 54(3):711–722
2. Bažant ZP, Luo W, Chau VT, Bessa MA (2016) Wave dispersion and basic concepts of peridynamics compared to classical nonlocal damage models. J Appl Mech 83(11):111004
3. Bobaru F, Duangpanya M (2010) The peridynamic formulation for transient heat conduction. Int J Heat Mass Transf 53(19-20):4047–4059
4. Butt SN, Timothy JJ, Meschke G (2017) Wave dispersion and propagation in state-based peridynamics. Comput Mech 60(5):725–738
5. Chen YM (1975) Numerical computation of dynamic stress intensity factors by a lagrangian finite-difference method (the hemp code). Eng Fract Mech 7(4):653–660
6. Diyaroglu C, Oterkus E, Oterkus S, Madenci E (2015) Peridynamics for bending of beams and plates with transverse shear deformation. Int J Solids Struct 69:152–168
7. Foster JT, Silling SA, Chen WW (2010) Viscoplasticity using peridynamics. Int J Numer Methods Eng 81(10):1242–1258
8. Foster JT, Silling SA, Chen W (2011) An energy based failure criterion for use with peridynamic states. Int J Multiscale Comput Eng 9(6):675–688
9. Gerstle W, Silling S, Read D, Tewary V, Lehoucq R (2008) Peridynamic simulation of electromigration. Computers Materials & Continua 8(2):75–92
10. Gu X, Zhang Q, Huang D, Yv Y (2016) Wave dispersion analysis and simulation method for concrete shpb test in peridynamics. Eng Fract Mech 160:124–137
11. Ha Y, Bobaru F (2009) Traction boundary conditions in peridynamics: a convergence study. Technical report, Department

of Engineering Mechanics, University of Nebraska–Lincoln, Lincoln, Nebraska
12. Ha YD, Bobaru F (2010) Studies of dynamic crack propagation and crack branching with peridynamics. Int J Fract 162(1-2):229–244
13. Han F, Lubineau G, Azdoud Y (2016) Adaptive coupling between damage mechanics and peridynamics: a route for objective simulation of material degradation up to complete failure. J Mech Phys Solids 94:453–472
14. Harari I (1997) Reducing spurious dispersion, anisotropy and reflection in finite element analysis of time-harmonic acoustics. Comput Methods Appl Mech Eng 140(1-2):39–58
15. Harari I, Turkel E (1995) Accurate finite difference methods for time-harmonic wave propagation. J Comput Phys 119(2):252–270
16. Jabakhanji R, Mohtar RH (2015) A peridynamic model of flow in porous media. Adv Water Resour 78:22–35
17. Kalthoff J (1973) On the propagation direction of bifurcated cracks. In: Proceedings of an international conference on dynamic crack propagation. Springer, pp 449–458
18. Liu ZL, Menouillard T, Belytschko T (2011) An XFEM/Spectral element method for dynamic crack propagation. Int J Fract 169(2):183–198
19. Madenci E, Oterkus E (2014) Peridynamic theory and its applications, vol 17. Springer, Berlin
20. Oterkus S, Madenci E, Agwai A (2014) Fully coupled peridynamic thermomechanics. J Mech Phys Solids 64:1–23
21. Ouchi H, Katiyar A, York J, Foster JT, Sharma MM (2015) A fully coupled porous flow and geomechanics model for fluid driven cracks: a peridynamics approach. Comput Mech 55(3):561–576
22. Seleson P (2014) Improved one-point quadrature algorithms for two-dimensional peridynamic models based on analytical calculations. Comput Methods Appl Mech Eng 282:184–217
23. Seleson P, Littlewood DJ (2016) Convergence studies in meshfree peridynamic simulations. Computers & Mathematics with Applications 71(11):2432–2448
24. Seleson P, Parks M (2011) On the role of the influence function in the peridynamic theory. Int J Multiscale Comput Eng 9(6):689–706
25. Seleson P, Beneddine S, Prudhomme S (2013) A force-based coupling scheme for peridynamics and classical elasticity. Comput Mater Sci 66:34–49
26. Silling SA (2000) Reformulation of elasticity theory for discontinuities and long-range forces. J Mech Phys Solids 48(1):175–209
27. Silling SA, Askari E (2005) A meshfree method based on the peridynamic model of solid mechanics. Comput Struct 83(17-18):1526–1535
28. Silling SA, Epton M, Weckner O, Xu J, Askari E (2007) Peridynamic states and constitutive modeling. J Elast 88(2):151–184
29. Tam CK, Webb JC (1993) Dispersion-relation-preserving finite difference schemes for computational acoustics. J Comput Phys 107(2):262–281
30. Weckner O, Abeyaratne R (2005) The effect of long-range forces on the dynamics of a bar. J Mech Phys Solids 53(3):705–728
31. Weckner O, Emmrich E (2005) Numerical simulation of the dynamics of a nonlocal, inhomogeneous, infinite bar. J Comput Appl Mech 6(2):311–319
32. Weckner O, Silling SA (2011) Determination of nonlocal constitutive equations from phonon dispersion relations. Int J Multiscale Comput Eng 9(6):623–634
33. Wildman RA, Gazonas GA (2014) A finite difference-augmented peridynamics method for reducing wave dispersion. Int J Fract 190(1-2):39–52
34. Wildman RA, OGrady JT, Gazonas GA (2017) A hybrid multiscale finite element/peridynamics method. Int J Fract 207(1):41–53
35. Zimmermann M (2005) A continuum theory with long-range forces for solids. PhD thesis, Massachusetts Institute of Technology